Journal of Materials Science: Materials in Electronics (2019) 30:6178–6186
https://doi.org/10.1007/s10854-019-00920-1

Impact of the annealing time on physical properties of sprayed In_2S_3 thin films

N. Bouguila[1] · M. Kraini[1] · A. Timoumi[2,3] · J. Koaib[1] · I. Halidou[4] · C. Vázquez-Vázquez[5]

Received: 9 November 2018 / Accepted: 11 February 2019 / Published online: 19 February 2019
© Springer Science+Business Media, LLC, part of Springer Nature 2019

Abstract
Indium sulfide thin films were deposited on preheated soda-lime glass substrates using spray technique over experiment optimum conditions ($T_s = 340$ °C, S/In = 2). The effect of annealing time on structural, morphological, optical and electrical properties of the films was investigated. X-ray diffraction spectra show that In_2S_3 films are polycrystalline with a cubic phase and preferentially oriented towards (400) for different annealing times. It is found that the film grain size increases from 39 to 49 nm when increasing the annealing time from 1 to 5 h. Both field emission scanning electron microscopy and atomic force microscopy images show that the surface morphology is strongly dependent upon the annealing time. Electron dispersive X-ray spectroscopy reveals that the film composition is not affected by the annealing. Raman spectroscopy analysis shows the predominance of active modes of β-In_2S_3 films with annealing time. Optical band gap is found to vary in the range 2.38–2.63 eV for direct transitions. At room temperature, Hall effect measurements show that the mobility (μ) and the carrier concentration (n_v) vary in the ranges 1.65–29.3 $cm^2\ V^{-1}\ s^{-1}$ and 1.16×10^{17}–2.82×10^{17} cm^{-3}, respectively. Also, the electrical resistivity of the films is reduced from 14.47 to 1.65 Ω cm with increasing annealing time. The results are in good agreement with available literature and showed its future use in many optoelectronics devices.

1 Introduction

In_2S_3 material is an important member of III–VI group semiconductors family. It is considered as a promising candidate for optoelectronic and photovoltaic applications [1–4]. In the literature, it is found that In_2S_3 crystallizes into three different structural forms α, β and γ which are growth temperature dependent [5, 6]. The β-In_2S_3 structure is the most stable phase at room temperature. It crystallizes in a normal spinel structure with a high degree of tetrahedral and octahedral vacancy sites [7, 8]. Such structure is characterized by a direct band gap semiconductor ranging from 2 to 3.7 eV [7]. The presence of a large number of defects destroys the periodicity of the lattice and distorts the crystal field. Therefore, the semiconducting character of these materials should be strongly affected by annealing process. The latter increases the degree of ordering and hence the material physical properties [9]. To improve the stability of deposited films and to reduce the possible undesirable influence of the substrate, a thermal treatment is usually used. Such process improves crystal quality and reduces structural defects in materials. The annealing process affects the dislocations and other structural defects. Accordingly, the structure and the stoichiometric ratio of the material will change due to the motion of defects and adsorption/decomposition will occur on the surface. Such phenomenon leads to major effects on semiconductor device properties [10–13].

It is well known that In_2S_3 thin films are prepared using several methods such as spray pyrolysis [12–17], ultrasonic dispersion [18], chemical bath deposition [19], physical vapor deposition [20], hydrothermal [21], etc. As the spray

✉ A. Timoumi
timoumiabdelmajid@yahoo.fr

1 Laboratoire de Physique des Matériaux et des Nanomatériaux appliquée à l'environnement, Faculté des Sciences de Gabès, Université de Gabès, Cité Erriadh Manara Zrig, 6072 Gabès, Tunisia

2 Department of Physics, Faculty of Applied Science, Umm AL-Qura University, 21955 Mecca, Saudi Arabia

3 Photovoltaic and Semiconductor Materials Laboratory, National Engineering School of Tunis, PO Box 37, Belvedere, 1002 Tunis, Tunisia

4 Département de Physique, Faculté des Sciences et Techniques, Université Abdou Moumouni, BP 10662, Niamey, Niger

5 Laboratory of Magnetism and Nanotechnology, Institute of Technological Research, Universidade de Santiago de Compostela, 15782 Santiago de Compostela, Spain

pyrolysis method allows preparing large area of thin films at low cost, it is chosen in the present work to conduct the preparation of In_2S_3 thin films. Then, we have investigated the effect of vacuum heat-treatment on some physical properties of In_2S_3 films. The annealing time effect on structural, morphological, optical and electrical properties of the prepared films were studied and discussed.

2 Experiment

The In_2S_3 films were deposited on glass substrates by using spray pyrolysis technique. The aqueous solution of pulverization contains indium(III) chloride $InCl_3$ and thiourea $SC(NH_2)_2$ as indium and sulphur precursors, respectively. Nitrogen was used as a carrier gas. The used solution composition is 10^{-2} mol l^{-1} of $InCl_3$ and 2×10^{-2} mol l^{-1} of $SC(NH_2)_2$. In_2S_3 material is obtained according to the chemical reaction described by the equation below:

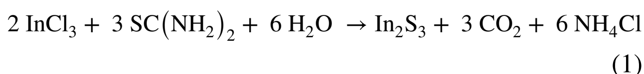

$$2\,InCl_3 + 3\,SC(NH_2)_2 + 6\,H_2O \rightarrow In_2S_3 + 3\,CO_2 + 6\,NH_4Cl \quad (1)$$

During the pulverization, the distance between the substrate and the jet is 20 cm. The solution and the nitrogen flows were fixed at 2 ml min^{-1} and 6 l min^{-1}, respectively. The sprayed time was 20 min. The obtained samples were sealed under vacuum in Pyrex tubes (10^{-5} Torr). Then they were heated at 340 °C for different annealing times (1, 2, 3, 4 and 5 h) according to the profile shown in Fig. 1.

The film crystalline structure was analyzed by X-ray diffraction (XRD) using CuK_α radiation (1.54186 Å). The surface morphology was investigated by means of field emission scanning electron microscopy (FESEM) using a Zeiss FESEM Ultra PLUS microscope, equipped with an energy dispersive X-ray spectroscopy detector (EDS) for chemical microanalysis, and by atomic force microscopy (AFM) using an XE-100 instrument (Park Systems Corporation) in non-contact mode (NC-AFM). Raman spectral measurements were carried out using a Raman spectrometer (Renishawin Via Reflex Spectrometer System) with an excitation wavelength of 514 nm. The transmittance and reflectance spectra were measured using a Shimadzu UV 3101 PC (spectrophotometer), with a wavelength range from 200 to 3000 nm, equipped with an integrating sphere. The resistivity, Hall mobility and carrier concentration were obtained from Hall effect measurements using the standard Van der Pauw configuration.

3 Results and discussion

3.1 Structural characterization

3.1.1 XRD analysis

Figure 2 shows the XRD patterns of In_2S_3 films annealed at 340 °C for various times (t_a). The films are polycrystalline and the crystallographic peaks belong to the cubic β-In_2S_3 phase with diffractions from (311), (400) and (511) planes, according to the JCPDS Card 32-0456. Impurity phases are not detected.

The peak intensities seem to change with increasing annealing time. Such observation indicates that the recrystallization process occurs during the annealing treatment.

The preferred orientations of In_2S_3 films were evaluated by the texture coefficient (TC), calculated from the X-ray data using the well-known formula:

$$TC(hkl) = \frac{I(hkl)/I_0(hkl)}{\frac{1}{N}\sum I(hkl)/I_0(hkl)} \quad (2)$$

where TC(*hkl*) is the texture coefficient of the (*hkl*) diffraction plane, I(*hkl*) is the measured or normalized intensity, I_0(hkl) is the corresponding standard intensity given in

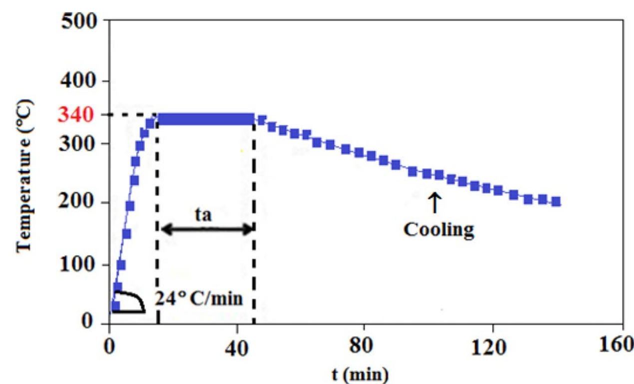

Fig. 1 Profile of annealing temperature evolution versus time

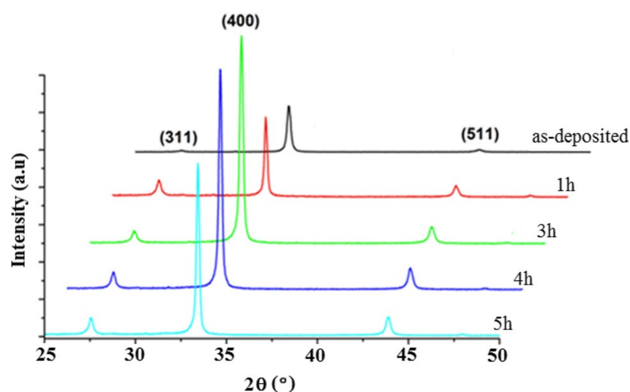

Fig. 2 X-ray diffraction patterns of as-deposited and annealed In_2S_3 films at 340 °C for different times

JCPDS data, and N is the number of reflections. The film preferred orientation will be (hkl) plane corresponding to the higher value of TC(*hkl*). TC(*hkl*) calculated for (311), (400) and (511) peaks were summarized in Table 1. The highest TC values are obtained for (400) plane for all the films.

Therefore, the film preferential orientation is (400). The (400) diffraction peak, for the film treated for 3 h, has the highest texture coefficient.

A rough estimate of the crystallite size (D) was made from X-ray diffraction data from (400) reflection by using the Scherer formula [22]:

$$D = \frac{0.9\lambda}{\beta \cos\theta} \tag{3}$$

where β is the size broadening in radians obtained as $\beta = \sqrt{\beta_e^2 - \beta_0^2}$, where β_e is the full width at half maximum of the diffraction peak and β_0 is the instrumental broadening (1.5×10^{-3} rd), λ is the wavelength of X-ray and θ is the Bragg angle.

The dislocation density (δ) is described as the length of dislocation lines per unit volume of the crystal [23]. The dislocation density gives information about the crystal structure. For the preferential orientation (400), such parameter can be calculated using the formula [24]:

$$\delta = \frac{1}{D^2} \tag{4}$$

Table 1 summarizes the calculated values of grain size and dislocation density of films.

It is observed that the grain size increases from about 39 to 49 nm with increasing of annealing time. Such observation can be related to the improvement of the film recrystallization [11, 25]. Similar results were recently reported by Avilez Garcia et al. [26]. The dislocation density decreases from 6.60×10^{10} to 4.16×10^{10} lines cm^{-2} with annealing time. Such behavior can be explained by the change of the grain size with annealing time. Indeed, the smaller crystallites have a greater surface to volume ratio. Hence, the dislocation density decreases with increasing annealing time which may be due to the decrease of lattice imperfections concentration [27].

3.1.2 Raman analysis

The Raman spectra of the films are shown in Fig. 3. The presence of β-In_2S_3 phase modes in all the films is noticed [28]. Indeed, the active modes of β-In_2S_3 observed at 139, 264, 312, and 368 cm^{-1} confirm the composition and the structure of the samples [29, 30]. The Raman modes are broad with low intensity. The film annealed for 3 h has a good crystallinity. The peak position and the half width of the β phase Raman bands exhibit independence upon the annealing time. However, there is a slight change in the relative intensities between the Raman bands at 264 and 312 cm^{-1} that seems to be correlated to the structural changes observed by X-ray diffraction.

3.2 Surface morphological and compositional analysis

Figure 4 illustrates 2D AFM images of In_2S_3 thin films annealed at 340 °C for different annealing time.

The effect of annealing time on the film morphology properties such as the surface average and RMS roughness are listed in Table 2. It is observed that the average and RMS

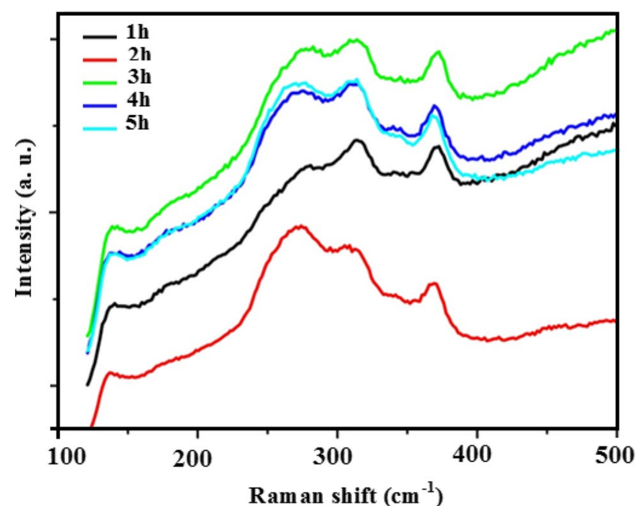

Fig. 3 Raman spectra of In_2S_3 thin films annealed at 340 °C at different times

Table 1 Crystallite size, dislocation density and texture coefficient for different annealing times

Annealing time (h)	D (nm)	δ (10^{10} lines cm^{-2})	TC (311)	TC (400)	TC (511)
As-deposited	38.90	6.60	0.12	2.65	0.12
1	43.31	5.33	0.39	2.38	0.23
3	48.97	4.16	0.12	2.73	0.13
4	47.41	4.44	0.16	2.66	0.17
5	47.72	4.39	0.19	2.63	0.18

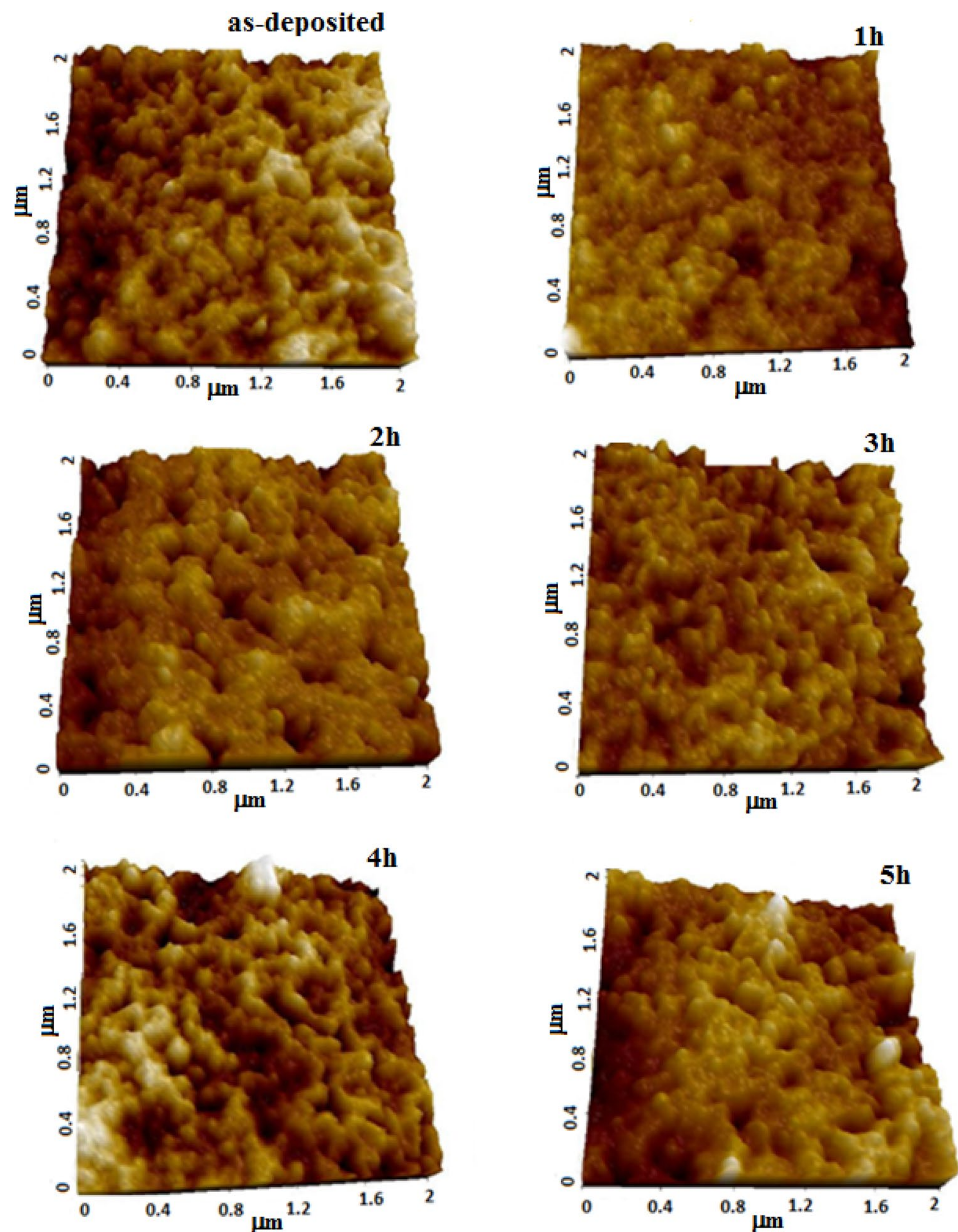

Fig. 4 2D AFM images of as-deposited and annealed In_2S_3 thin films at 340 °C with different times

Table 2 Average and RMS roughness of In_2S_3 thin films annealed at 340 °C for various annealing times, obtained from the AFM images

Annealing time (h)	RMS (nm)	Ra (nm)
As-deposited	8.94	7.08
1	10.22	7.81
2	8.70	6.59
3	8.24	6.40
4	9.23	7.18
5	13.31	10.47

roughness values decrease with the annealing time increase up to 3 h.

However, the surface becomes rougher as the annealing time is increased to 4 h and 5 h. An increase of the surface roughness may be due to the structural modification produced by the increase of annealing time. The film crystallites become larger leading to the obtention of larger surface roughness [26, 31]. The films surface morphology was also studied by FESEM. The typical FESEM images for different annealing times, are depicted in Fig. 5. These images show that the morphology of the investigated films has larger number of grain size and are homogeneously distributed. It is also observed that the grains are formed in cubic structure with void space between the grains. FESEM image of

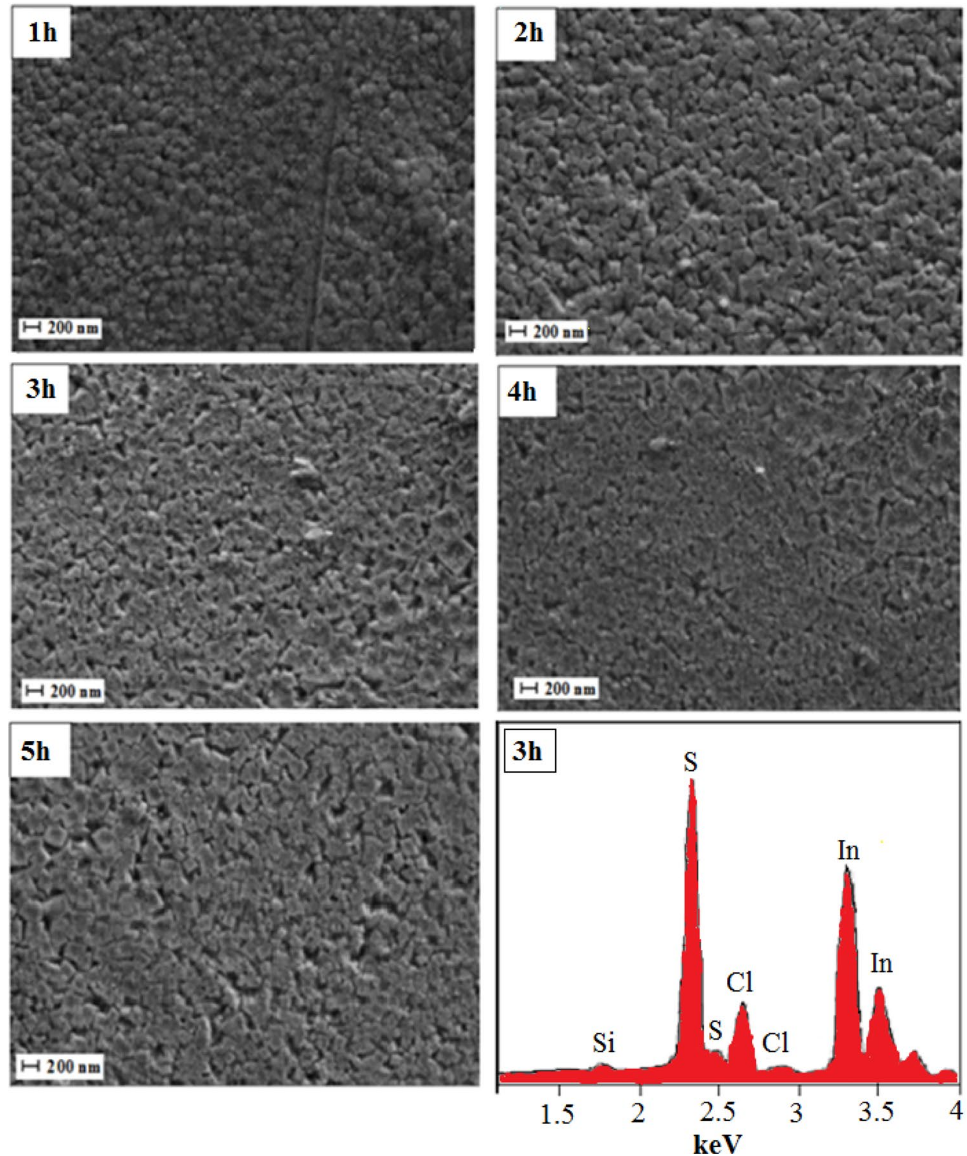

Fig. 5 FESEM images of In_2S_3 thin films prepared at 340 °C with different annealing times (1 h, 2 h, 3 h, 4 h and 5 h) and EDS spectrum of In_2S_3 films annealed at 340 °C for 3 h

In_2S_3 film, annealed for 1 h, shows that the particles exhibit a small size. As the annealing time increases to 3 h, the particles size increases. Thus, the particle size, of the In_2S_3 films, increases rapidly with increasing the annealing time. FESEM results confirm the increase of grain size increasing annealing time as revealed by XRD measurements.

For the investigated samples, annealed for different times, the chemical composition was studied using EDS analysis. The obtained results are given in Table 3. A typical EDS graph, for selected sample, is also shown in Fig. 4. It is observed that the atomic ratio S/In is not sensible to the increase of annealing time. Its average value is in order of 1.4. Such value is lower than the molar ratio in the initial solution (S/In = 2) and the stoichiometric one (S/In = 1.5). This deviation is probably due to the volatility of sulfur. It can be concluded that the annealing time has not a significant influence on the stoichiometry of the formed In_2S_3 layers.

Table 3 Atomic contents in In_2S_3 thin films annealed for various times characterized by EDS technique

Annealing time (h)	S (at.%)	In (at.%)	S/In
As-deposited	57.51	42.49	1.35
1	57.25	42.75	1.35
2	58.33	41.67	1.39
3	58.83	41.17	1.43
4	58.77	41.23	1.42
5	58.01	41.99	1.39

3.3 Optical properties

3.3.1 Optical transmittance and reflectance spectra

Figure 6 shows the spectral distributions of both the transmission (T) and the reflection (R) at normal incidence with annealing time. For 1 h annealing, the transmission decreases to a saturation value of about 65% (Fig. 6a). When the annealing duration exceeds 1 h the film transparency is not remarkably affected. We point out the presence of the interference fringes due to the multitude reflection phenomena showing homogenous films. However, this decrease occurs mainly in transmission, while reflection is almost not affected (Fig. 6b). Moreover, these films exhibit a good transparency in the visible and infrared regions. The films are transparent of about 70%, and the total reflection (R) remains nearly at the same value of about 20% for all films. In general, the optical transmittance is influenced mainly by the film thickness, the surface morphology as well as the grain density and defects at the grain boundaries [11, 32].

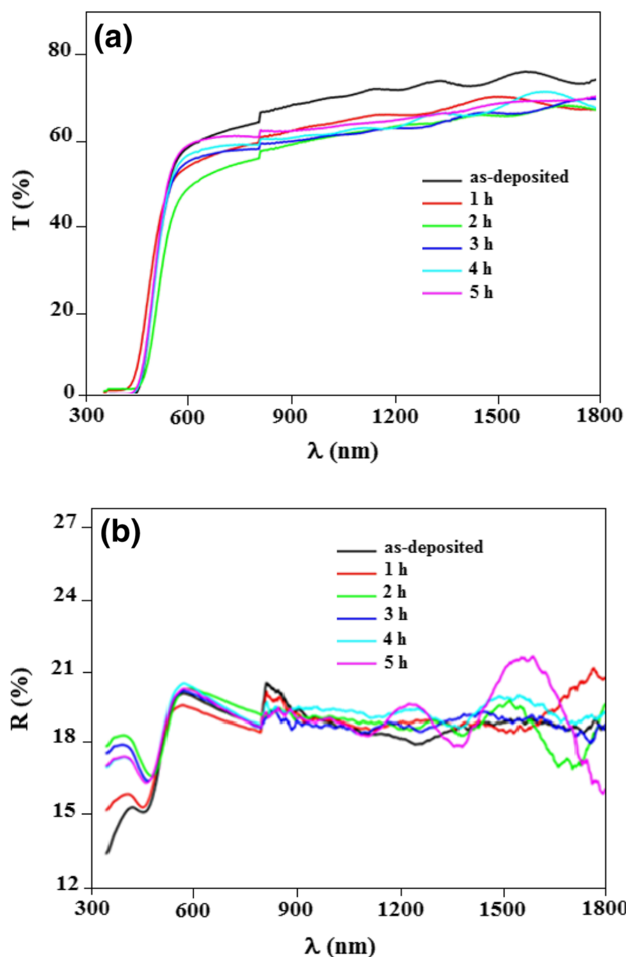

Fig. 6 Optical transmission (**a**) and reflection (**b**) spectra of as deposited and annealed In_2S_3 films treated at 340 °C as a function of annealing time

3.3.2 Refractive index and thickness

The film thicknesses were calculated from the positions of the interference maxima and minima of transmittance spectra using a standard method. The refractive index can be calculated by using the maxima (T_{max}) and the minima (T_{min}) of the envelopes of the transmission spectra [33] given on Fig. 6. The expression of refractive index is given by [34]:

$$n = (N + (N^2 - {n_0}^2{n_1}^2)^{\frac{1}{2}})^{\frac{1}{2}} \tag{5}$$

where

$$N = \frac{{n_0}^2 + {n_1}^2}{2} + 2n_0n_1\frac{T_{\max} - T_{\min}}{T_{\max}T_{\min}} \tag{6}$$

n_0, n_1 are the refractive index of air and substrate, respectively.

The thickness (d) was given by [35]:

$$d = \frac{\lambda_1\lambda_2}{2(n(\lambda_1)\lambda_2 - n(\lambda_2)\lambda_1)} \tag{7}$$

The evolution of the thickness and the average refractive index of the layers with annealing time are illustrated in Fig. 7. We notice that the layers become thinner by increasing the annealing time. This fact can be explained by the grains coalescence. Also, in the region of transparency, the annealing time has not a remarkable effect on the refractive index of the samples.

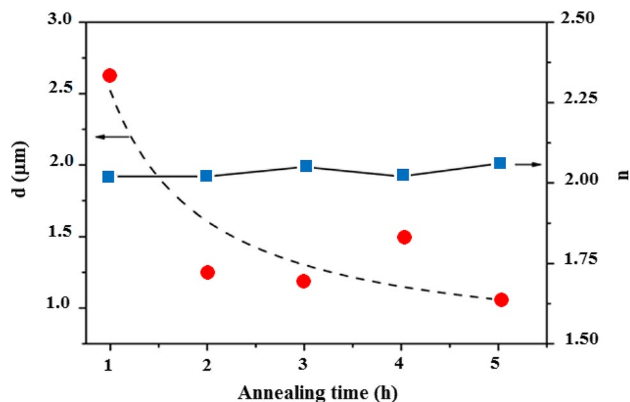

Fig. 7 Evolution of refractive index and thickness as a function of annealing times

3.3.3 Band gap energy

The film absorption coefficient (α) was calculated using the equation:

$$\alpha = -\frac{1}{d}\ln\frac{T}{1-R^2} \quad (8)$$

The analysis of the absorption coefficient, in the high absorption region is carried out to obtain the detailed information about the band gap energy. The optical band gap of the films is inferred using the following relation [11]:

$$\alpha h\nu = A(h\nu - E_g)^n \quad (9)$$

where A is a constant, α is the absorption coefficient, hν is the photon energy, E_g is the optical band gap and the exponent (n) characterizes the nature of band transition. Indeed, n = 1/2 and 2 correspond to direct allowed and indirect forbidden transitions, respectively. Figure 8 shows the variation of $(\alpha h\nu)^2$ against (hν). The band gap energy is determined by extrapolating the straight line portion to the energy basis at α = 0. We observe that the curve has a very good straight line fit.

The films exhibit a direct band gap varying from 2.63 to 2.38 eV as a function of annealing time. Moreover, the band gap energy could also be influenced by the variation of particle size with annealing time as it is in the nanometer range. Though, it is not close to the Bohr radius. Therefore, in the present study, the increase of grain size by the agglomeration of particles, leads to the decrease of band gap energy of the films with increasing annealing time [36]. Indeed, as revealed by the XRD patterns and AFM images, the films undergo a crystallization process during the annealing route. Similar variation of band gap energy was observed by Revathi et al. [37]. The measured E_g values are lower than those reported in reference [38]. In the literature, large variations of the band gap of indium sulphide films were reported [39–42]. Such type of variation is generally attributed to structural effects. It was observed that the band gap energy has the highest value for 1 h heat treated thin film. Then it decreases with increasing annealing time up to 2 h. However, for samples annealed for more than 2 h, the band gap energy increases with annealing time. Such result can be related to the enhancement of the realignment in orientation and strong interaction between the substrate and vapor atoms [43].

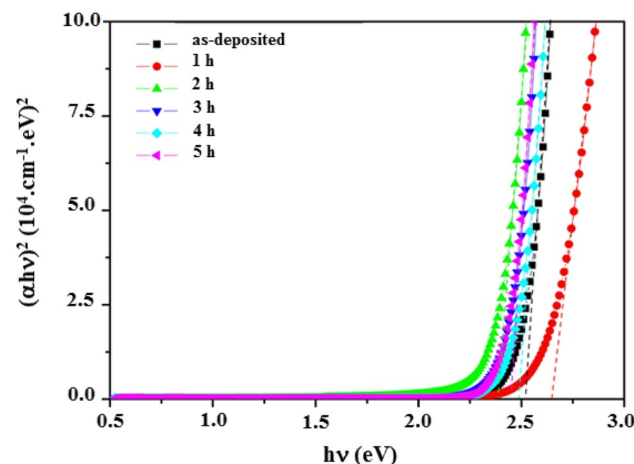

Fig. 8 Dependence of $(\alpha h\nu)^2$ versus hν for as deposited and annealed of In_2S_3 thin films at different annealing times

3.4 Electrical properties

The resistivity, the carrier concentration and the mobility values of the In_2S_3 thin films annealed at different time were evaluated by Hall measurement system at room temperature. The corresponding values were listed in Table 4. The carrier concentration (n_v) is derived from the relation $n_v = \frac{1}{e.R_H}$ [44], where R_H is the Hall coefficient and e is the absolute value of the electron charge. The carrier mobility (μ) is determined using the relation $\mu = \frac{1}{en_v\rho}$, where ρ is the resistivity [45].

All films exhibit n-type conductivity which means that the annealing time did not change the type of the majority carriers. Moreover, the mobility and the carrier concentration vary in the range 1.65–29.3 $cm^2\ V^{-1}\ s^{-1}$ and 1.16×10^{17}–$2.82\times10^{17}\ cm^{-3}$, respectively. The mobility increases as a result of reconstituting and the crystallinity prosperity of the material. The carrier concentration variation is probably due to the variation of sulfur vacancies. The electrical resistivity of the films decreases from 14.47 to 1.65 Ω cm when annealing time increases. Such decrease is consistent with the results observed from XRD diffractograms. Indeed, the increase of grain size during the annealing process results in a smaller effect of grain boundary leading to a reduction of the films resistivity. The noticed reduction of the electrical resistivity is proven to be quite advantageous for photovoltaic applications.

Table 4 Resistivity, carrier concentration and mobility of In_2S_3 films annealed at 340 °C as a function of annealing time

Annealing time (h)	μ ($cm^2\ V^{-1}\ s^{-1}$)	n_v ($10^{17}\ cm^{-3}$)	ρ (Ω cm)
1	1.65	2.61	14.47
2	29.30	2.82	0.75
3	15.02	1.16	3.58
4	9.20	2.60	2.60
5	25.30	1.50	1.65

4 Conclusions

In this work, we report the effect of annealing time on sprayed In_2S_3 films deposited under optimum conditions ($T_s = 340$ °C, S/In = 2) and annealed in vacuum at different times (1 h, 2 h, 3 h, 4 h and 5 h). Results showed that the annealing duration ameliorates the films crystallinity and their orientation. The obtained films were polycrystalline with cubic crystal structure and with preferential orientation (400). The film thickness decreases from 2.7 to 1 µm with annealing time but the refractive index is not sensitive to such factor. The grain size increases from 39 to 49 nm with the annealing time. Also, the morphology and the crystallinity of the films are strongly influenced. Raman spectroscopy confirms the presence of β-In_2S_3 phase for all films. The films are transparent in the visible (80%). The values of optical band gap were evaluated and were found to be ranged between 2.63 and 2.38 eV with the annealing time. The carrier concentration and the mobility vary in the ranges 1.16×10^{17}–2.82×10^{17} cm^{-3} and 1.65–29.3 cm^2 V^{-1} s^{-1}, respectively. The electrical resistivity of the films decreases from 14.47 to 1.65 Ω cm, indicating an improvement of the conductivity. Annealed films with these properties may be promising material for optoelectronic applications.

Acknowledgements This work was supported by Tunisian Ministry of Higher Education and Scientific Research and MINECO, Spain (Project MAT2012-36754-C02-01, MAT2015-67458-P); Xunta de Galicia, Spain (Grupos Ref. Comp. GRC2013-044, FEDER Funds). The authors would like to thank Pr. A. Belhadj Amara (Faculté des Sciences de Bizerte, Université de Carthage, Tunisie) for XRD measurements and Dr. H. Rahmouni (ISSAT Kasserine, Université de Kairouan, Tunisie) for Hall effect measurements.

References

1. M. Mathew, M. Gopinath, C.S. Kartha, K.P. Vijayakumar, Y. Kashiwaba, T. Abe, Sol. Energy **84**, 888 (2010)
2. T.T. John, M. Mathew, C.S. Kartha, K.P. Vijayakumar, T. Abe, Y. Kashiwaba, Sol. Energy. Mater. Sol. Cells **89**, 27 (2005)
3. M. Kilani, B. Yahmadi, N.K. Turki, M. Castagné, J. Mater. Sci. **46**, 6293 (2011)
4. S. Siebentritt, Sol. Energy **77**, 767 (2004)
5. S. Cingarapu, M.A. Ikenberry, D.B. Hamal, C.M. Sorensen, K. Hohn, K.J. Klabunde, Langmuir **28**, 3569 (2012)
6. L.J. Liu, W.D. Xiang, J.S. Zhong, X.Y. Yang, X.J. Liang, H.T. Liu, W. Cai, J. Alloys Compd. **493**, 309 (2010)
7. N. Barreau, Sol. Energy **83**, 363 (2009)
8. H. Spasevska, C.C. Kitts, C. Ancora, G. Ruani, Int. J. Photoenergy. **2012**, 637943 (2012)
9. K. Kambas, J. Spyridelis, Mater. Res. Bull. **13**, 653 (1978)
10. A. Timoumi, H. Bouzouita, R. Brini, M. Kanzari, B. Rezig, Appl. Surf. Sci. **253**, 306 (2006)
11. M. Kraini, N. Bouguila, I. Halidou, A. Timoumi, S. Alaya, Mater. Sci. Semicond. Process. **16**, 1388 (2013)
12. N. Bouguila, A. Timoumi, H. Bouzouita, Eur. Phys. J. Appl. Phys. **65**, 20304 (2014)
13. M. Kraini, N. Bouguila, J. El Ghoul, I. Halidou, S.A. Gomez-Lopera, C. Vázquez-Vázquez, M.A. López-Quintela, S. Alaya, J. Mater. Sci. Mater. Electron. **2**, 5774 (2015)
14. N. Bouguila, A. Timoumi, H. Bouzouita, E. Lacaze, H. Bouchriha, B. Rezig, Eur. Phys. J. Appl. Phys. **63**, 20301 (2013)
15. N. Bouguila, I. Najeh, N. Ben Mansour, H. Bouzouita, S. Alaya, J. Mater. Sci. Mater. Electron. **26**, 6471 (2015)
16. M. Hasan Zadeh Maha, M.M. Bagheri-Mohagheghi, H. Azimi-Juybari, Thin Solid Films **536**, 57 (2013)
17. M. Mathew, R. Jayakrishnan, P.M. Ratheesh Kumar, C. Sudha Kartha, K.P. Vijayakumar, T. Abe, Y. Kashiwaba, J. Appl. Phys. **100**, 033504 (2006)
18. Z. Li, X. Tao, Z. Wu, P. Zhang, Z. Zhang, Ultrason. Sonochem. **16**, 221 (2009)
19. B. Asenjo, C. Sanz, C. Guillén, A.M. Chaparro, M.T. Gutiérrez, J. Herrero, Thin Solid Films **515**, 6041 (2007)
20. N. Barreau, J.C. Bernède, C. Deudon, L. Brohan, S. Marsillac, Thin Solid Films **241**, 4 (2002)
21. P.G.S. Abadi, M.S. Niasari, F. Davar, Superlattice Microstruct. **53**, 76 (2013)
22. B.D. Cullity, *Elements of X-ray Diffraction* (Addison-Wesley, Reading, 1978)
23. K. Ravichandran, P. Philominathan, Sol. Energy **82**, 1062 (2008)
24. V. Bilgin, S. Kose, F. Atay, I. Akyuz, Mater. Chem. Phys. **94**, 103 (2005)
25. M. Oztas, M. Bedir, Z. Ozturk, D. Korkmaz, S. Sur, Chin. Phys. Lett. **23**, 1610 (2006)
26. R.G. Avilez Garcia, C.A. Meza, M. Avendaño, F. Pal, N.R. Paraguay Delgado, Mathews, Mater. Sci. Semicond. Process. **44**, 91 (2016)
27. N. Nagarani, J. Photonics Spintron. **2**, 19 (2013)
28. L. Aldon, M. Uhrmacher, C. Branci, L. Ziegler, J. Roth, P. Schaaf, H. Metzner, J. Olivier-Fourcade, J.C. Jumas, Phys. Rev. B **58**, 11303 (1998)
29. K. Kambas, J. Spyridelis, M. Balkanski, Phys. Status Solidi **105**, 291 (1981)
30. H. Tao, H. Zang, G. Dong, J. Zeng, X. Zhao, Optoelectron. Adv. Mater. **2**, 356 (2008)
31. A.L. Barabasi, H.E. Stanley, *Fractal Concepts in Surface Growth* (Cambridge University Press, Cambridge, 1995)
32. A. Larena, F. Millan, G. Perez, G. Pinto, App. Surf. Sci. **187**, 339 (2002)
33. S.H. Wemple, M. Di Domenico, Phys. Rev. B **143**, 1338 (1971)
34. A. Timoumi, H. Bouzouita, B. Rezig, Thin Solid Films **519**, 761 (2011)
35. A. Boukhachema, B. Ouni, M. Karyaoui, A. Madani, R. Chtourou, M. Amlouk, Mater. Sci. Semicond. Process. **15**, 282 (2012)
36. R. Rusdi, A.A. Rahman, N.S. Mohamed, N. Kamarudin, N. Kamarulzaman, Powder Technol. **210**, 18 (2011)
37. N. Revathi, P. Prathap, R.W. Miles, K.T. Reddy, Sol. Energy. Mater. Sol. Cells **94**, 1487 (2010)
38. C. Guillén, T. Garcia, J. Herrero, M.T. Gutiénrez, F. Brions, Thin Solid Films **112**, 451 (2004)
39. N. Bouguila, M. Kraini, A. Timoumi, I. Halidou, C. Vázquez-Vázquez, M.A. López-Quintela, S. Alaya, J. Mater. Sci. **26**, 7639 (2015)
40. N. Bouguila, M. Kraini, I. Halidou, E. Lacaze, H. Bouchriha, H. Bouzouita, J. Electron. Mater. **45**, 829 (2016)
41. C.D. Lakhande, A. Ennaoui, P.S. Patil, M. Giersi, K. Diesner, M. Muller, H. Tributsch, Thin Solid Films **340**, 18 (1999)
42. Z. Gao, J. Liu, H. Wang, Mat. Sci. Semicond. Process. **15**, 187 (2012)

43. S. Lalitha, R. Sathyamoorthy, S. Senthilarasu, A. Subbarayan, K. Natarajan, Sol. Energy Mater. Sol. Cells. **82**, 187 (2004)
44. B.A. Cook, J.L. Harringa, J. App. Phys. **83**, 5858 (1998)
45. M. Nisha, S. Anusha, A. Antony, R. Manoj, M.K. Jayaraj, Appl. Surf. Sci. **252**, 1430 (2005)

Publisher's Note Springer Nature remains neutral with regard to jurisdictional claims in published maps and institutional affiliations.